High-temperature superconductivity of boron-carbon clathrates at ambient pressure

Junda Li,[1,*] Jincheng Yue,[1,*] Siqi Guo,[1] Ao Zhang,[2] Li Zhu,[3] Hao Song,[1] Zhao Liu,[1] Yanhui Liu,[1,†] and Tian Cui[1,4,‡]

[1]*Institute of High-Pressure Physics, School of Physical Science and Technology, Ningbo University, Ningbo 315211, China*

[2]*School of Physics, Southeast University, Nanjing 211189, China*

[3]*Department of Physics, Rutgers University, Newark, New Jersey 07102, USA*

[4]*State Key Laboratory of Superhard Materials, College of Physics, Jilin University, Changchun 130012, China*

(Received 16 October 2023; revised 7 February 2024; accepted 13 March 2024; published 9 April 2024)

The successful synthesis of the carbon-boron clathrate SrB_3C_3 under high-pressure conditions of 50 GPa opens up a new possibility for exploring high-temperature superconductors at ambient pressure. Based on the first-principle calculation, we designed a class of LaH_{10}-like clathrate compounds $Fm\bar{3}m$-XB_2C_8 (X = K, Rb, Cs, Sr, Ba, Ga, In, Tl, Sn, Pb, and Bi) and investigate their physical properties and potential superconductivities. Our calculations reveal that the dynamic stability of $Fm\bar{3}m$-XB_2C_8 at ambient pressure is determined by the degree of compatibility between the host metal X and the carbon-boron sublattices. Especially, p orbitals of the p-region metals can enhance the interaction of the guest atoms with B-C cages, which results in maintaining these clathrates as dynamically stable. Moreover, altering the oxidation states of the guest atoms can adjust the electronic density of states near the Fermi surface, which in turn affects the superconducting transition temperatures (T_c's) of these compounds. Herein, when filled with +1 oxidation state metals, the T_c's of XB_2C_8 (X = K, Rb, Cs, Ga, In, and Tl) all exceed the liquid-nitrogen boiling point of 77 K and the T_c of TlB_2C_8 is expected to reach 96 K at ambient pressure, which is the highest among the studied carbon-boron compounds.

DOI: 10.1103/PhysRevB.109.144509

I. INTRODUCTION

Superconductivity has been one of the central topics in condensed-matter physics due to its unique phenomena and promising applications [1–9]. Since the past century, unconventional superconductors represented by YBaCuO [1–3], HgBaCaCuO [4–6], and $La_3Ni_2O_7$ [10] have achieved superconducting transition temperatures (T_c's) above the boiling point of liquid nitrogen. However, the lack of understanding of the mechanism underlying superconductivity impedes the further development of these materials. In the field of conventional superconductors, clathrate hydrides such as CaH_6 [11,12], CeH_9 [13,14], and LaH_{10} [15–17] have been theoretically predicted and experimentally confirmed based on the Bardeen-Cooper-Schrieffer theory [18] and the "chemical precompression" theory [19]. In these hydrides, electrons donated by guest metals fill the antibonding orbitals of hydrogen, causing H atoms to form caged skeletons connected by weak covalent bonds, rather than appearing as H_2 units [11,15]. The average distances of H-H bonds are close to the theoretical metal-hydrogen bond lengths, resulting in near-room temperature superconductivity [15,17]. Unfortunately, the weakened H-H covalent bonds also require extremely high pressures to stabilize these metallic hydrides, which seriously limits their synthesis and practical applications. [11–17,20]. Therefore, searching for new superconducting materials with clear superconductivity mechanisms that are stable under ambient pressure becomes the next challenge in the field of superconductivity.

Boron and carbon are the lightest elements capable of forming strong covalent bonds, for which materials based on these elements are expected to exhibit strong covalent bonding/antibonding states across the Fermi energy level (E_F) [21,22]. These states can effectively interact with phonons, thus giving rise to potentially strong electron-phonon-coupling (EPC) superconductivity [22–29]. A prominent example of this scenario is the conventional superconducting compound MgB_2, which exhibits a T_c of 39 K at ambient pressure, owing to the strong coupling of σ electrons located in the antibonding state with phonons [23,24]. Inspired by these observations, several potential conventional superconductors with strong EPC have been suggested, including CaC_6 [25], YbC_6 [25], YB_6 [26], NaC_6 [22], BaB_3C_3 [28], and the recently experimentally synthesized SrB_3C_3 [27–29]. Notably, SrB_3C_3 and BaB_3C_3 represent a promising class of B-C compounds in which the B-C cage skeletons resemble the H_{24} cages of the well-known binary hydrogen-rich compound CaH_6. This can be considered as substituting H atoms with equal proportions of B and C atoms in the cage backbone of CaH_6. Guest metals with appropriate oxidation states provide additional electrons to the B-C skeleton, where the high density of electronic states near the E_F and the lattice vibrations result in strong EPC, leading to superconductivity [27–29].

Recent studies on nonhydrogen cage compounds, which have a structure akin to CaH_6, indicate that replacing the H atoms in common hydride cages with light elements can

*These authors contributed equally to this work.

†liuyanhui@nbu.edu.cn

‡cuitian@nbu.edu.cn

effectively lead to the discovery of new stable superconductors at ambient pressures [22,27–33]. These findings hint at a new realm for delving into high-T_c superconductors. With the vast array of cagelike structures available, there is a promising avenue to explore potential superconductors grounded in alternative cage designs. For example, LaH_{10} represents another well-known cage hydride with high-temperature superconductivity and a T_c higher than that of CaH_6 [11,12,15–17], which implies that LaH_{10}-based B-C cage compounds may exhibit better superconductivity potential at ambient pressure. In view of the above analysis, we propose a class of boron-carbon clathrates $Fm\bar{3}m$-XB_2C_8 (X = K, Rb, Cs, Sr, Ba, Ga, In, Tl, Sn, Pb, and Bi) by replacing two types of H atoms in the H_{32} cage of LaH_{10} with boron and carbon and investigate their crystal structure properties, dynamical stability, and possible superconductivity at ambient pressure. We find 11 dynamically stable structures, including 9 metals and 2 nonmetals. The calculation results indicate that the electronic density of states at the E_F and T_c of XB_2C_8 can be tuned by changing the oxidation states of the guest metal atoms. Estimated from the Allen-Dynes modified McMillan equation, the T_c of XB_2C_8 exceeds the boiling temperature of liquid nitrogen when filled with +1 oxidized metal X (X = K, Rb, Cs, Ga, In, and Tl). More interestingly, TlB_2C_8 shows a T_c of 96 K, which to our knowledge, is the highest of the known boron-carbon compounds at ambient pressure. Our research reveals a class of high-temperature superconducting materials at ambient pressure with potential applications, which enriches the components of B-C superconducting materials and will facilitate the exploration of conventional superconductivity.

II. COMPUTATIONAL METHODS

Our first-principle calculations, including structural geometry optimization, phonon dispersion, molecular dynamics simulations, and electronic structure calculations, were implemented in the Vienna Ab initio Simulation Package (VASP) based on density-functional theory [34,35], with the Perdew-Burke-Ernzerhof generalized gradient approximation [36] of the projector-augmented-wave method [37]. The cutoff energy of the plane-wave was set to 800 eV. In the structural optimization process, the convergence thresholds were 10^{-7} eV for energy and 10^{-3} eV/Å for force, with the Monkhorst-Pack k-point spacing distribution of 0.03 $Å^{-1}$. The Heyd-Scuseria-Ernzerhof (HSE06) hybrid function [38] was used to evaluate the band structures and density of states (DOS), and, for the heaviest sixth-period elemental compounds, the effect of spin-orbit coupling (SOC) on their energy bands was considered. Phonon dispersion calculations were performed on $2 \times 2 \times 2$ supercells containing 88 atoms utilizing the VASP package coupled to the PHONOPY code [39,40]. Interactions in the crystal structure were analyzed by the MULTIWFN 3.8 program for interaction region indicators (IRIs) based on reduced density gradients [41,42]. All IRI maps were rendered by the VMD 1.9.3 program [43]. For compounds exhibiting metals, a higher accuracy of phonon dispersion and EPC calculations were performed with the QUANTUM ESPRESSO software package [44]. Ultrasoft pseudopotentials for all elements were used with a kinetic energy

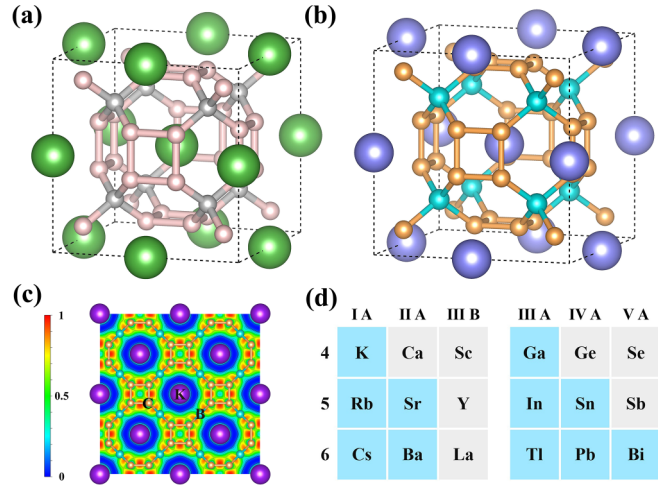

FIG. 1. (a) The crystal structure of $Fm\bar{3}m$-LaH_{10}. La atoms are shown in green, and two different kinds of H atoms are shown in pink and gray. (b) The crystal structure of $Fm\bar{3}m$-XB_2C_8 (X = K, Rb, Cs, Sr, Ba, Ga, In, Tl, Sn, Pb, and Bi). X atoms are shown in violet, B atoms are shown in cyan, and C atoms are shown in orange. (c) Calculated ELF of $Fm\bar{3}m$-KB_2C_8 at 0 GPa. (d) Periodic table of the stability for $Fm\bar{3}m$-XB_2C_8 at ambient pressure, with columns indicating the major groups of elements and rows indicating periods, where dynamically unstable compounds in phonon calculations at atmospheric pressure are shown in gray and stable compounds are shown in blue.

cutoff of 80 Ry. A k mesh of $18 \times 18 \times 18$ and a q mesh of $6 \times 6 \times 6$ for structures in the first Brillouin zone were adopted in the EPC calculations. The superconducting critical temperature was estimated from the self-consistent solution of the Allen-Dynes-corrected McMillan equation [45], expressed as

$$T_c = f_1 f_2 \frac{\omega_{\log}}{1.2} \exp\left[-\frac{1.04(1+\lambda)}{\lambda - \mu^*(1+0.62\lambda)}\right], \quad (1)$$

where μ^* denotes the Coulomb pseudopotential, taken as $\mu^* = 0.1$–0.13 in our calculations. $\omega_{\log}$ is the logarithmic average of the phonons, expressed as

$$\omega_{\log} = \exp\left[\frac{2}{\lambda}\int_0^\infty \frac{\alpha^2 F(\omega)}{\omega} d\omega\right]. \quad (2)$$

The electron-phonon coupling constant λ was expressed as

$$\lambda = 2\int_0^\infty \frac{\alpha^2 F(\omega)}{\omega} d\omega. \quad (3)$$

III. RESULTS AND DISCUSSION

Drawing inspiration from the renowned superhydride superconductor $Fm\bar{3}m$-LaH_{10} [15–17], we propose a class of carbon-boron clathrate materials. The distinctive H_{32} backbone of LaH_{10} features two types of nonidentical H atoms, which occupy the 8c and 32f Wyckoff positions. These atoms surround the metal atoms situated at the cage centers, forming conventional host-guest structures as depicted in Fig. 1(a). We have devised model structures by replacing B and C atoms within the $Fm\bar{3}m$-LaH_{10} framework.

Considering the extremely large number of potential substitutions (on the order of 2^{32}) for the LaH_{10} lattice, we employ a computationally manageable approach to this challenge. We assume fixed symmetry of the structure and only make substitutions of atoms on special framework Wyckoff positions. We maintain the symmetry of the structure and solely focus on atom substitutions at specific framework Wyckoff positions. Using this method, we replace the two kinds of distinct H atoms with light nonmetallic elements B and C.

After full optimization of the structure at ambient pressure, we derive $Fm\bar{3}m$-XB_2C_8, where X denotes different guest metals [Fig. 1(b)]. Unlike SrB_3C_3 and other CaH_6-like materials, the new B-C clathrates retain LaH_{10} structural features. For each B-C cage, 24 C atoms form 6 C_4 squares, while 8 B atoms are connected to the adjacent C_4 units, resulting in 12 C_4B_2 hexagonal planes. The B and C atoms form the interconnected framework, while the guest metal atoms occupy the center of the cubic unit. We compute the electron localization function (ELF) to investigate the electron distribution and bonding interactions in XB_2C_8. The B-C framework is bonded with polar strong covalent bonds formed by sp^3 hybridization, which is a major factor for the stability of XB_2C_8 at ambient pressure. As an example, the values of ELF between the B-C and C-C atoms are larger than 0.75 for KB_2C_8, indicating strong interactions between the atoms [Fig. 1(c)]. There is no electron localization between the K atom and the B-C backbone, which implies that the guest metal K shows pure ionic bonding.

Having ascertained the structures of the new ternary B-C compounds, we further investigated the dynamical stability of $Fm\bar{3}m$-XB_2C_8 for 18 different elements as guest atoms [Fig. 1(d)]. Our results indicate that 11 compounds are dynamically stable at ambient pressure, including 9 metals (X = K, Rb, Cs, Ga, In, Tl, Sn, Pb, and Bi) as well as 2 nonmetals (X = Sr, Ba) (see Figs. S1– S3 in the Supplemental Material [46]). All these stable compounds share the same symmetry as $Fm\bar{3}m$-LaH_{10} and the B-C sublattices are connected in covalent bonds. The B-C bond lengths range from 1.65 to 1.70 Å, while the C-C bond lengths range from 1.59 to 1.61 Å, which indicates that changing the inserted metal atoms at ambient pressure has little effect on the size of the B-C sublattice.

Interestingly, we find that with decreasing atomic radius of the guest metals, the dynamic stability of XB_2C_8 at ambient pressure gradually declines (Fig. 1(d), Table S1 [46]). For the alkali-metal compounds with the largest atomic radii, KB_2C_8, RbB_2C_8, and CsB_2C_8 are kinetically stable at atmospheric pressure. However, as the guest atomic radius decreases, the phonon spectrum of the alkaline-earth-metal compound CaB_2C_8 exhibits imaginary frequencies, which indicates a loss of structural stability (see Fig. S1 in the Supplemental Material [46]). We have not found a structure that remains stable at ambient pressure for the neighboring group III B elements with smaller radii. Interestingly, this stability rule is also consistent with previous reports on materials such as XB_3C_3 [21,30] and XB_3Si_3 [31], which demonstrate the importance of favorable matching between boron carbide cages and internal metal atoms [21,22,27–31]. Noticeably, for the guest metal X, although the average atomic radius of the elements in the p region (from group III A to group V A of the periodic table of the elements) is much smaller than that of Ca, Sc, Y, and La, which form kinetically unstable compounds at atmospheric pressure, a similar kinetic stability law still applies to the p-region elements (Fig. 1(d) and Fig. S2 [46]).

To investigate the origin of the anomalous stabilities of metallic borocarbides in the p region, we calculated the IRIs [41] (Fig. 2). This method measures the strength of the interaction by ρ (electron density), which allows different colors to distinguish the regions and types of interactions. Figure 2 displays the IRIs of six representative compounds of period 6, illustrating the strength of the weak interaction forces and the region of action. This allows for further analysis of the potential interactions between the boron-carbon cage and the metal atoms. For the stable CsB_2C_8, the deep blue isosurfaces between the B-C and C-C bonds correspond to covalent bonding. The green isosurfaces around Cs atoms suggest a weak interaction force between guest metals and the B-C sublattice, comparable to the van der Waals force, while the coexistence of light red areas also reveals the presence of a steric effect. A state of approximate equilibrium between the weak interaction and steric effects enables CsB_2C_8 to remain dynamically stable at atmospheric pressure. However, the matching of metal atoms to B-C cages deteriorates with the decreasing size of metal atoms in the same period [Figs. 2(a)–2(c)]. Particularly for LaB_2C_8, the red region representing the steric effect is significantly intensified, disrupting the original equilibrium state and making the compound unstable. Significantly, this imbalance can be restored by applying external pressure. When the pressure is increased to 100 GPa, the B-C sublattice in LaB_2C_8 is compressed, resulting in a size reduction, and both $r_{B\text{-}C}$ and $r_{C\text{-}C}$ bond lengths are shortened to 1.55 Å. Phonon dispersion shows that the LaB_2C_8 becomes dynamically stable at 100 GPa (see the phonon dispersion curves for LaB_2C_8 at 0 and 100 GPa in Figs. S4(c) and S4(d) of the Supplemental Material [46]). Compared to the IRI at 0 GPa, the weak interaction region of LaB_2C_8 at 100 GPa is noticeably darker, implying an improved match between the metal atoms and the B-C cage (see the isosurface map of IRIs of LaB_2C_8 at 0 and 100 GPa in Figs. S4(a) and S4(b) of the Supplementary Material [46]). For p-region elements, a smaller average atomic radius leads to a stronger steric effect [Figs. 2(d)–2(f)], but near the guest metal, the equivalence surface with a bluer color indicates a stronger interaction of the p-region metal with the B-C cage, which enables the delicate equilibrium relationship to be reconstructed.

Figure 3 shows the oxidation states of metals and the effect of p-region metals on the electronic properties of the compounds, where the electronic band structures and partial density of states (PDOS) for the six most representative compounds are displayed, grouped by period (Cs, Ba, La, Tl, Pb, and Bi), and the remaining are shown in Fig. S3 in the Supplemental Material [46]. For guest metals X with Cs, Ba, and adjacent La, the energy band of $Fm\bar{3}m$-XB_2C_8 exhibits a clear rigid-band model: the valence band regions are mainly derived by the B-C sublattices and their shape is barely influenced by the inserted X atoms. The metal X with different oxidation

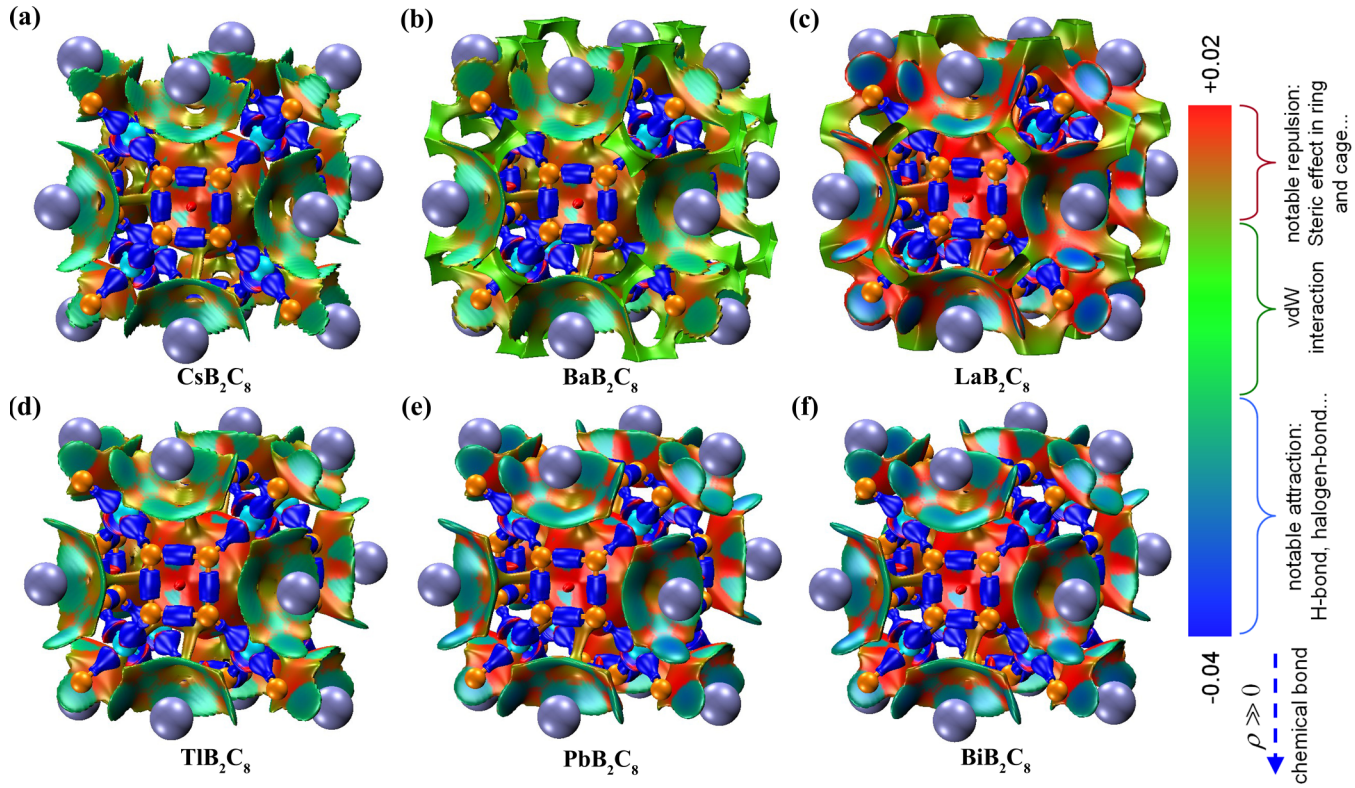

FIG. 2. Isosurface map of interaction region indicator (IRI) of (a) CsB_2C_8, (b) BaB_2C_8, (c) LaB_2C_8, (d) TlB_2C_8, (e) PbB_2C_8, and (f) BiB_2C_8, at 1 atm, using the standard coloring method and chemical explanation of sign(λ_2) ρ on IRI isosurfaces.

states is almost fully ionized and transfers charges to the B-C sublattice, occupying its electron orbitals and thus shifting the energy level of the E_F. As a result, when Cs atoms with a +1 oxidation state are inserted, the E_F traverses the valence band and approaches a peak in the DOS composed almost entirely of the electrons from C and B atoms. The high DOS

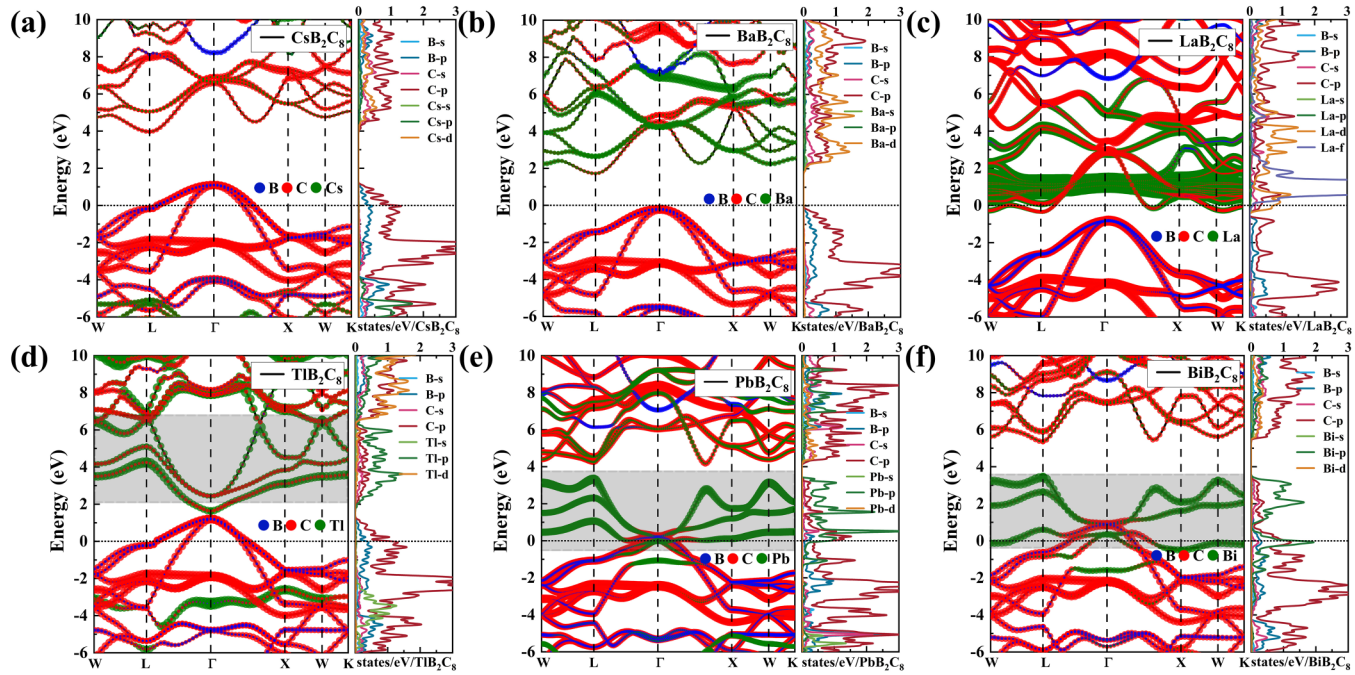

FIG. 3. Calculated electronic band structures and projected density of states (PDOS) for (a) CsB_2C_8, (b) BaB_2C_8, (c) LaB_2C_8, (d) TlB_2C_8, (e) PbB_2C_8, and (f) BiB_2C_8 at atmospheric pressure by using HSE06 + SOC where the E_F is set to zero. The total densitis of states for B, C, and guest metals projected onto the energy band are shown with blue, red, and green points, respectively.

peak at E_F originates from the Van Hove singularity near the high symmetry point L and is crucial to improving the possibility of forming Cooper pairs in CsB_2C_8, which enhances the EPC strength and superconductivity [Fig. 3(a)]. When Sr and Ba atoms with +2 oxidation state are inserted, the borocarbide cage receives almost fully ionized electrons from the alkaline-earth metal to form the $X^{2+}[B_2C_8]^{2-}$ formula, leading to an upward shift of the E_F into the forbidden band region and producing an insulator (Fig. 3(b) and Fig. S3 [46]). When filling with La atoms in the +3 state, the E_F continues to rise and crosses the conduction band, forming an electron-doped conductor [Fig. 3(c)].

Elements in the p region usually have multiple oxidation states, such as the toxic element Pb, which has +2 and +4 as its most common oxidation states [21]. By performing the Bader charge transfer analysis [47,48], we find that in compounds XB_2C_8 the metals from groups III A and IVA exhibit +1 and +2 oxidation states, respectively (Table S2). This means that the energy band structure of TlB_2C_8 behaves similarly to that of CsB_2C_8, but a higher DOS near the E_F indicates a greater potential for superconductivity [Figs. 3(a) and 3(d)]. It is worth noting that when p-region elements are inserted, the 6p orbitals of guest metals create a distinct interaction region with the 2p orbitals of C atoms [gray shaded region in Figs. 3(d)–3(f)]. This also confirms that the p-region guest metals and B-C cages can form interactions similar to weak π-bonds, thus keeping XB_2C_8 dynamically stable at atmospheric pressure (X = Ga, In, Tl, Sn, Pb, and Bi). By replacing the guest metals from Tl to Pb and Bi, with the increase of atomic number, more electrons fill into the p orbitals of the guest metals, resulting in a decrease of the energy of the interacting electron band and a gradual strengthening of the weak π-bonds [Figs. 3(d)–3(f)]. At the same time, the lowered electron bands cross the E_F and hybridize with the top of valence bands, which causes the metallization of PbB_2C_8 and BiB_2C_8.

For investigating the potential superconductivity properties of 9 ternary B-C compounds that show metallic behavior at ambient pressure, we used the Allen-Dynes-modified McMillan equation to estimate the T_c's, logarithmic average phonon frequency $\omega_{\log}$ (K), and electron density N_{EF} at the E_F (states/eV/f.u.), as shown in Fig. 4 and Table S3 [46]. The superconductivity of XB_2C_8 compounds can be broadly divided into two types based on their metallization. On the one hand, for structures filled with +1 oxidation metals (X = K, Rb, Cs, Ga, In, and Tl), the E_F crosses the valence bands and creates hole-type conductors, resulting in the T_c's of all these phases being above the liquid-nitrogen boiling-point temperature. For the phases containing group IA metals, their λ ranges from 1.34 to 1.51 and $\omega_{\log}$ from 734 to 765 K, leading to T_c's in the range of 85–92 K ($\mu^* = 0.1$). When containing metals from group III A, though the $\omega_{\log}$ of these phases drops to around 650 K, higher N_{EF} and λ values keep even slightly enhanced values of T_c's. Notably, TlB_2C_8 has a T_c of 96 K, which exceeds $KPbB_6C_6$ (88 K) predicted by Geng *et al.* [21] and is the highest among our analyzed systems. On the other hand, for phases involving metals in the p region with +2 or higher oxidation states, the metallization is dominated by guest metals and increases with the increase in the p orbitals of the metals. For group IVA SnB_2C_8 and PbB_2C_8, the low

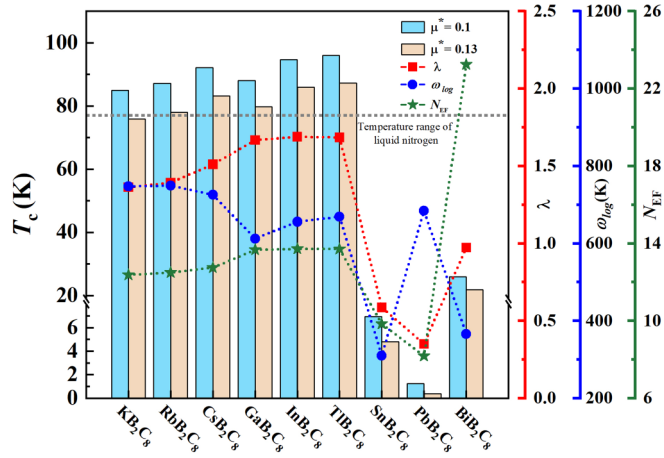

FIG. 4. Calculated superconducting parameters for $Fm\bar{3}m$-XB_2C_8 (X = K, Rb, Cs, Ga, In, Tl, Sn, Pb, and Bi). T_c's calculated by Allen-Dynes-modified equations ($\mu^* = 0.1$–0.13), $\omega_{\log}$, λ, and N_{EF} at the E_F. The gray dashed line in the picture is the liquid-nitrogen boiling-point temperature.

DOS near the EF decreases the electron-phonon interaction drastically, resulting in their λ values being less than 0.6 and their T_c's being less than 8 K. In our calculations, although BiB_2C_8 has the highest N_{EF}, the heavy Bi atom severely limits the λ value, and the value of T_c is less than that of the first class of structures, which is only 25 K.

To further explore the origin of this strong EPC, we plotted the phonon spectrum, phonon density of states (PHDOS), and integral EPC parameter λ for all identified superconducting phases (Fig. S5 [46]). It is worth noting that superconducting phases can be classified into four groups based on the main group of the inserted metallic elements. The phonon spectra of metallic superconducting phases within the same main group are very similar. Therefore, we selected the four most representative superconducting phase phonon spectra, as shown in Fig. 5. For all considered phases, the phonon spectrum can be divided into two regions: the low-frequency region around 3 THz dominated by the vibrations of the heavy guest metal atoms (green peaks in PHDOS), and the high-frequency region arising from boron and carbon vibrations (red and blue peaks in PHDOS). CsB_2C_8 and TlB_2C_8 with high T_c's of over 90 K have a very similar phonon spectral structure [Figs. 5(a) and 5(b)]. The integral curve of λ grows rapidly in the 12–20 THz range, corresponding to the red region in the phonon spectrum and the two distinct peaks in the Eliashberg spectral function. The peaks in the 12–15 THz interval are almost entirely attributed to C optical phonons, corresponding to the telescopic vibrations of the ortho-tetragonal C loops, while for the peaks at higher frequencies in the 16–20 THz range, the ratio of B to C optical phonon contributions is about 2:3, corresponding to the contractive and bending vibrations of the hexagonal B-C loops. In the case of PbB_2C_8 with the lowest T_c [Fig. 5(c)], the electron-phonon coupling of optical phonons is low, and the contribution to λ is concentrated in the high-frequency region above 20 THz. In Fig. 5(d), the metal Bi in BiB_2C_8 contributes significantly to the Eliashberg spectral function with a contribution of about 34%. Compared to TlB_2C_8, which has the highest T_c value, BiB_2C_8 lacks

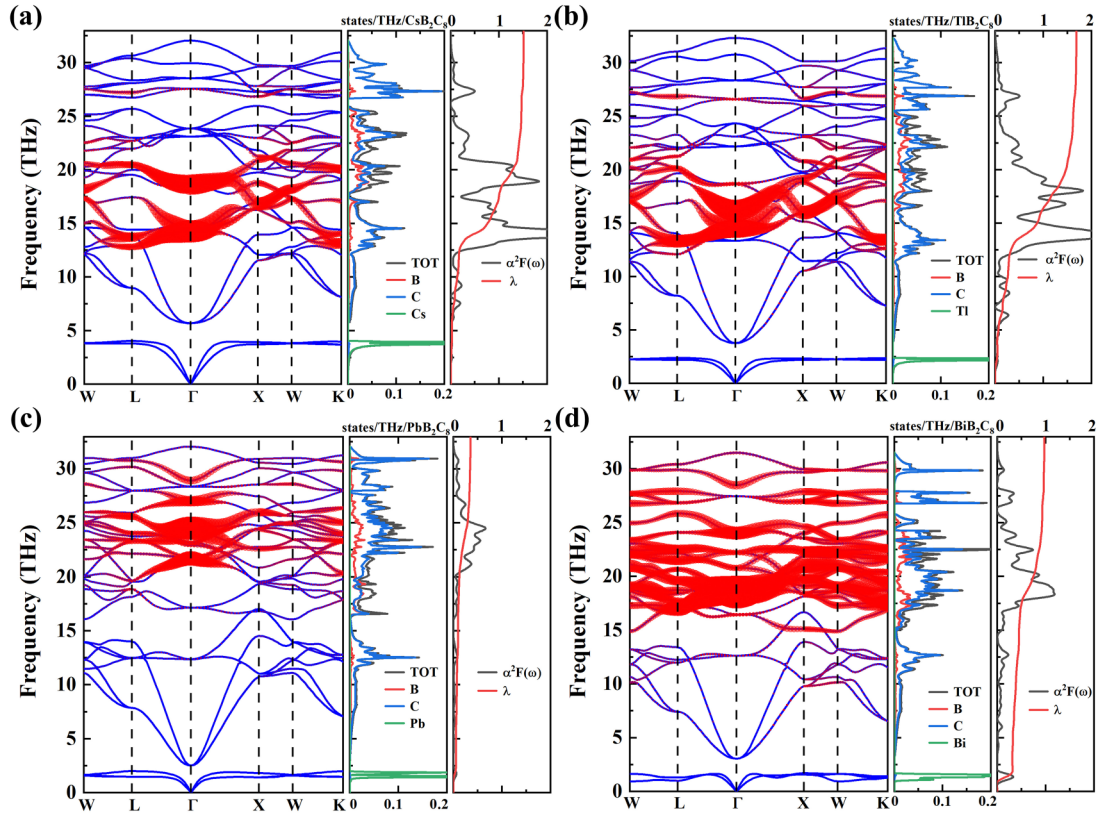

FIG. 5. Phonon dispersion curves, projected phonon density of states, Eliashberg spectral function scaled by the frequency $[\alpha^2 F(\omega)]$, and the EPC integral (λ) for (a) CsB_2C_8, (b) TlB_2C_8, (c) PbB_2C_8, and (d) BiB_2C_8 at 0 GPa. The bubble's radius on the phonon dispersion curve is proportional to the electron-phonon coupling constant (λ).

the electroacoustic coupling contribution in the 12–15 THz interval, which results in a value of λ only slightly above 1. Eventually, the T_c of BiB_2C_8 fails to exceed the McMillan limit.

Finally, we performed molecular dynamics simulations of the stable 11 structures using the NPT system synthesis [49]. The results show that all the structures (except BiB_2C_8) have good structural energy stability at 300 K and 1 atm (see Fig. S6 in the Supplemental Material [46]), and their kinetic barriers prevent the structures from decomposing under ambient conditions. In addition, we further investigated the thermodynamic stability of KB_2C_8 by assuming several possible decomposition pathways, like the elemental phase, BC_3 [50], K_2C_2 [51], and KC_8 [52,53], and systematically studied the enthalpy of formation as a function of pressure. Figure S7 in the Supplemental Material [46] shows the enthalpy differences for several selected reaction paths in the 0–50 GPa pressure range. Even though the enthalpy difference for the decomposition of KB_2C_8 into elemental phases at 25 GPa exceeds 340 meV/atom, this still does not completely exclude the possibility of synthesizing such cagelike B-C compounds. It was reported that compounds such as SiB_6 and C_{60} were successfully synthesized experimentally [54,55], while the calculated formation energies reached 289 meV/atom [56]and 350 meV/atom [57] for them, respectively.

Additionally, experimental method improvements can also facilitate the synthesis of suitable materials. For example, Guan *et al.* successfully demonstrated the possibility of synthesizing synthetic Li-Mg-H substable hydrogen-rich compounds using the pressure-potential method at moderate pressure [58]. Gao *et al.* applied plastic shear in their experiments and succeeded in reducing the pressure and temperature conditions for synthesizing diamond to 0.7 GPa and 300 K, which is about 2 orders of magnitude lower than the transformation pressure under quasihydrostatic conditions [59]. Encouragingly, we note that the enthalpy of production of KC_8 at 45 GPa is higher than that of KB_2C_8, which implies that the B-C material can be synthesized by this particular reaction route under certain conditions.

IV. CONCLUSIONS

In conclusion, we have identified a class of boron-carbon clathrates $Fm\bar{3}m$-XB_2C_8 (X = K, Rb, Cs, Sr, Ba, Ga, In, Tl, Sn, Pb, and Bi), which has a cage structure similar to the typical hydride LaH_{10} and is dynamically stable at atmospheric pressure, including nine metals and two semiconductors. IRI calculations show that the stability of XB_2C_8 depends on the guest metal radius and oxidation state; with decreasing radius and increasing oxidation state, the rising potential resistance effect weakens the interaction between the guest metal and the B-C sublattice, making the structure unstable. For compounds containing metals with smaller average atomic radii in the p region, the p orbital of the guest atom strengthens the interaction with the B-C sublattice, counteracting the additional repulsive forces due to the potential resis-

tance effect and stabilizing the compound. As estimated from the Allen-Dynes-modified McMillan equation, at atmospheric pressure, T_c's of XB_2C_8 with filled oxidation states of $+1$ metal all surpass the boiling temperature of liquid nitrogen, with TlB_2C_8 reaching 96 K, the highest of our boron-carbon compounds. Our study presents a class of atmospheric pressure high-temperature superconducting materials with high potential applications, which will further promote theoretical exploration in the field of conventional superconductors and provide a reference for the experimental synthesis of new conventional superconductors.

ACKNOWLEDGMENTS

This work was supported by the National Natural Science Foundation of China (Grants No. 52072188 and No. 12204254), the Program for Science and Technology Innovation Team in Zhejiang (Grant No. 2021R01004), and the Natural Science Foundation of Zhejiang Province (Grant No. LQ23A040005). We are grateful to the Institute of High-Pressure Physics of Ningbo University for its computational resources.

There are no conflicts to declare.

[1] J. Z. Sun, D. J. Webb, M. Naito, K. Char, M. R. Hahn, J. W. P. Hsu, A. D. Kent, D. B. Mitzi, B. Oh, M. R. Beasley, T. H. Geballe, R. H. Hammond, and A. Kapitulnik, Superconductivity and magnetism in the high-T_c superconductor YBaCuO, Phys. Rev. Lett. **58**, 1574 (1987).

[2] J. Geerk, G. Linker, and O. Meyer, Epitaxial growth and properties of YBaCuO thin films, Mater. Sci. Rep. **4**, 193 (1989).

[3] M. Murakami, Processing of bulk YBaCuO, Supercond. Sci. Technol. **5**, 185 (1992).

[4] A. Schilling, M. Cantoni, J. Guo, and H. Ott, Superconductivity above 130 K in the Hg–Ba–Ca–Cu–O system, Nature (London) **363**, 56 (1993).

[5] Z. Iqbal, T. Datta, D. Kirven, A. Lungu, J. C. Barry, F. J. Owens, A. G. Rinzler, D. Yang, and F. Reidinger, Superconductivity above 130 K in the Hg-Pb-Ba-Ca-Cu-O system, Phys. Rev. B **49**, 12322 (1994).

[6] Y. Li, V. Balédent, N. Barišić, Y. Cho, B. Fauqué, Y. Sidis, G. Yu, X. Zhao, P. Bourges, and M. Greven, Unusual magnetic order in the pseudogap region of the superconductor $HgBa_2CuO_{4+\delta}$, Nature (London) **455**, 372 (2008).

[7] D. Duan, Y. Liu, F. Tian, D. Li, X. Huang, Z. Zhao, H. Yu, B. Liu, W. Tian, and T. Cui, Pressure-induced metallization of dense $(H_2S)_2H_2$ with high-T_c superconductivity, Sci. Rep. **4**, 6968 (2014).

[8] M. Du, H. Song, Z. Zhang, D. Duan, and T. Cui, Room-temperature superconductivity in Yb/Lu substituted clathrate hexahydrides under moderate pressure, Research **2022**, 9784309 (2022).

[9] W. Zhao, H. Song, Z. Liu, M. Du, Z. Zhang, Z. Liu, Q. Jiang, L. Chen, D. Duan, and T. Cui, Pressure induced clathrate hydrogen-rich superconductors KH_{20} and KH_{30}, Inorg. Chem. **61**, 18112 (2022).

[10] H. Sun, M. Huo, X. Hu, J. Li, Z. Liu, Y. Han, L. Tang, Z. Mao, P. Yang, B. Wang *et al.*, Signatures of superconductivity near 80 K in a nickelate under high pressure, Nature (London) **621**, 493 (2023).

[11] H. Wang, J. S. Tse, K. Tanaka, T. Iitaka, and Y. Ma, Superconductive sodalite-like clathrate calcium hydride at high pressures, Proc. Natl. Acad. Sci. USA **109**, 6463 (2012).

[12] L. Ma, K. Wang, Y. Xie, X. Yang, Y. Wang, M. Zhou, H. Liu, X. Yu, Y. Zhao, H. Wang *et al.*, High-temperature superconducting phase in clathrate calcium hydride CaH_6 up to 215 K at a pressure of 172 GPa, Phys. Rev. Lett. **128**, 167001 (2022).

[13] X. Li, X. Huang, D. Duan, C. J. Pickard, D. Zhou, H. Xie, Q. Zhuang, Y. Huang, Q. Zhou, B. Liu *et al.*, Polyhydride CeH_9 with an atomic-like hydrogen clathrate structure, Nat. Commun. **10**, 3461 (2019).

[14] N. P. Salke, M. M. Davari Esfahani, Y. Zhang, I. A. Kruglov, J. Zhou, Y. Wang, E. Greenberg, V. B. Prakapenka, J. Liu, A. R. Oganov *et al.*, Synthesis of clathrate cerium superhydride CeH_9 at 80–100 GPa with atomic hydrogen sublattice, Nat. Commun. **10**, 4453 (2019).

[15] H. Liu, I. I. Naumov, R. Hoffmann, N. Ashcroft, and R. J. Hemley, Potential high-T_c superconducting lanthanum and yttrium hydrides at high pressure, Proc. Natl. Acad. Sci. USA **114**, 6990 (2017).

[16] M. Somayazulu, M. Ahart, A. K. Mishra, Z. M. Geballe, M. Baldini, Y. Meng, V. V. Struzhkin, and R. J. Hemley, Evidence for superconductivity above 260 K in lanthanum superhydride at megabar pressures, Phys. Rev. Lett. **122**, 027001 (2019).

[17] A. Drozdov, P. Kong, V. Minkov, S. Besedin, M. Kuzovnikov, S. Mozaffari, L. Balicas, F. Balakirev, D. Graf, V. Prakapenka *et al.*, Superconductivity at 250 K in lanthanum hydride under high pressures, Nature (London) **569**, 528 (2019).

[18] J. Bardeen, L. N. Cooper, and J. R. Schrieffer, Theory of superconductivity, Phys. Rev. **108**, 1175 (1957).

[19] N. W. Ashcroft, Hydrogen dominant metallic alloys: High temperature superconductors?, Phys. Rev. Lett. **92**, 187002 (2004).

[20] N. W. Ashcroft, Metallic hydrogen: A high-temperature superconductor?, Phys. Rev. Lett. **21**, 1748 (1968).

[21] N. Geng, K. P. Hilleke, L. Zhu, X. Wang, T. A. Strobel, and E. Zurek, Conventional high-temperature superconductivity in metallic, covalently bonded, binary-guest C-B clathrates, J. Am. Chem. Soc. **145**, 1696 (2023).

[22] S. Lu, H. Liu, I. I. Naumov, S. Meng, Y. Li, J. S. Tse, B. Yang, and R. J. Hemley, Superconductivity in dense carbon-based materials, Phys. Rev. B **93**, 104509 (2016).

[23] J. Kortus, I. I. Mazin, K. D. Belashchenko, V. P. Antropov, and L. L. Boyer, Superconductivity of metallic boron in MgB_2, Phys. Rev. Lett. **86**, 4656 (2001).

[24] J. Nagamatsu, N. Nakagawa, T. Muranaka, Y. Zenitani, and J. Akimitsu, Superconductivity at 39 K in magnesium diboride, Nature (London) **410**, 63 (2001).

[25] T. E. Weller, M. Ellerby, S. S. Saxena, R. P. Smith, and N. T. Skipper, Superconductivity in the intercalated graphite compounds C_6Yb and C_6Ca, Nat. Phys. **1**, 39 (2005).

[26] S. Kunii, T. Kasuya, K. Kadowaki, M. Date, and S. Woods, Electron tunneling into superconducting YB_6, Solid State Commun. **52**, 659 (1984).

[27] L. Zhu, G. M. Borstad, H. Liu, P. A. Guńka, M. Guerette, J.-A. Dolyniuk, Y. Meng, E. Greenberg, V. B. Prakapenka, B. L. Chaloux *et al.*, Carbon-boron clathrates as a new class of *sp*3-bonded framework materials, Sci. Adv. **6**, eaay8361 (2020).

[28] J.-N. Wang, X.-W. Yan, and M. Gao, High-temperature superconductivity in SrB_3C_3 and BaB_3C_3 predicted from first-principles anisotropic Migdal-Eliashberg theory, Phys. Rev. B **103**, 144515 (2021).

[29] L. Zhu, H. Liu, M. Somayazulu, Y. Meng, P. A. Guńka, T. B. Shiell, C. Kenney-Benson, S. Chariton, V. B. Prakapenka, H. Yoon *et al.*, Superconductivity in SrB_3C_3 clathrate, Phys. Rev. Res. **5**, 013012 (2023).

[30] P. Zhang, X. Li, X. Yang, H. Wang, Y. Yao, and H. Liu, Path to high-T_c superconductivity via Rb substitution of guest metal atoms in the SrB_3C_3 clathrate, Phys. Rev. B **105**, 094503 (2022).

[31] T.-T. Gai, P.-J. Guo, H.-C. Yang, Y. Gao, M. Gao, and Z.-Y. Lu, Van hove singularity induced phonon-mediated superconductivity above 77 K in hole-doped SrB_3C_3, Phys. Rev. B **105**, 224514 (2022).

[32] S. Di Cataldo, S. Qulaghasi, G. B. Bachelet, and L. Boeri, High-T_c superconductivity in doped boron-carbon clathrates, Phys. Rev. B **105**, 064516 (2022).

[33] X. Cui, K. P. Hilleke, X. Wang, M. Lu, M. Zhang, E. Zurek, W. Li, D. Zhang, Y. Yan, and T. Bi, RbB_3Si_3: An alkali metal borosilicide that is metastable and superconducting at 1 atm, J. Phys. Chem. C **124**, 14826 (2020).

[34] G. Kresse and J. Furthmüller, Efficient iterative schemes for *ab initio* total-energy calculations using a plane-wave basis set, Phys. Rev. B **54**, 11169 (1996).

[35] G. Kresse and J. Furthmüller, Efficiency of ab-initio total energy calculations for metals and semiconductors using a plane-wave basis set, Comput. Mater. Sci. **6**, 15 (1996).

[36] J. P. Perdew, K. Burke, and M. Ernzerhof, Generalized gradient approximation made simple, Phys. Rev. Lett. **77**, 3865 (1996).

[37] G. Kresse and D. Joubert, From ultrasoft pseudopotentials to the projector augmented-wave method, Phys. Rev. B **59**, 1758 (1999).

[38] A. V. Krukau, O. A. Vydrov, A. F. Izmaylov, and G. E. Scuseria, Influence of the exchange screening parameter on the performance of screened hybrid functionals, J. Chem. Phys. **125**, 224106 (2006).

[39] K. Parlinski, Z. Q. Li, and Y. Kawazoe, First-principles determination of the soft mode in cubic ZrO_2, Phys. Rev. Lett. **78**, 4063 (1997).

[40] L. Chaput, A. Togo, I. Tanaka, and G. Hug, Phonon-phonon interactions in transition metals, Phys. Rev. B **84**, 094302 (2011).

[41] T. Lu and F. Chen, Multiwfn: A multifunctional wavefunction analyzer, J. Comput. Chem. **33**, 580 (2012).

[42] T. Lu and Q. Chen, Interaction region indicator: A simple real space function clearly revealing both chemical bonds and weak interactions, Chem. Methods **1**, 231 (2021).

[43] S. Manzetti and T. Lu, The geometry and electronic structure of aristolochic acid: Possible implications for a frozen resonance, J. Phys. Org. Chem. **26**, 473 (2013).

[44] P. Giannozzi, O. Baseggio, P. Bonfà, D. Brunato, R. Car, I. Carnimeo, C. Cavazzoni, S. De Gironcoli, P. Delugas, F. Ferrari Ruffino *et al.*, Quantum ESPRESSO toward the exascale, J. Chem. Phys. **152**, 154105 (2020).

[45] P. B. Allen and R. Dynes, Transition temperature of strong-coupled superconductors reanalyzed, Phys. Rev. B **12**, 905 (1975).

[46] See Supplemental Material at http://link.aps.org/supplemental/10.1103/PhysRevB.109.144509 for data on phonon dispersion, energy band structure, superconductivity calculations, structural parameters, and molecular dynamics simulations of the XB_2C_8 clathrate structures, which includes Refs. [60,61].

[47] G. Henkelman, A. Arnaldsson, and H. Jónsson, A fast and robust algorithm for Bader decomposition of charge density, Comput. Mater. Sci. **36**, 354 (2006).

[48] M. Yu and D. R. Trinkle, Accurate and efficient algorithm for Bader charge integration, J. Chem. Phys. **134**, 064111 (2011).

[49] S. Nosé, A unified formulation of the constant temperature molecular dynamics methods, J. Chem. Phys. **81**, 511 (1984).

[50] M. Zhang, H. Liu, Q. Li, B. Gao, Y. Wang, H. Li, C. Chen, and Y. Ma, Superhard BC_3 in cubic diamond structure, Phys. Rev. Lett. **114**, 015502 (2015).

[51] S. Hemmersbach, B. Zibrowius, and U. Ruschewitz, Na_2C_2 und K_2C_2: Synthese, kristallstruktur und spektroskopische eigenschaften, Z. Anorg. Allg. Chem. **625**, 1440 (1999).

[52] P. Lagrange, D. Guerard, and A. Hérold, Ann. Chim. (Paris, Fr.) **3**, 143 (1978).

[53] D. Guerard, P. Lagrange, M. El Makrini, and A. Hérold, Etude structurale du graphiture I de cesium, Carbon **16**, 285 (1978).

[54] M. Vlasse, G. A. Slack, M. Garbauskas, J. S. Kasper, and J. C. Viala, The crystal structure of SiB_6, J. Solid State Chem. **63**, 31 (1986).

[55] H. W. Kroto, J. R. Heath, S. C. Obrien, C. F. Curl, and R. E. Smalley, Long carbon chain molecules in circumstellar shells, Astrophys. J. **314**, 352 (1987).

[56] Z. Yuan, M. Xiong, and D. Yu, A novel metallic silicon hexaboride, *Cmca*-B_6Si, Phys. Lett. A **384**, 126075 (2020).

[57] J.-T. Wang, H. Weng, S. Nie, Z. Fang, Y. Kawazoe, and C. Chen, Body-centered orthorhombic C_{16}: A novel topological node-line semimetal, Phys. Rev. Lett. **116**, 195501 (2016).

[58] P.-W. Guan, Y. Sun, R. J. Hemley, H. Liu, Y. Ma, and V. Viswanathan, Low-pressure electrochemical synthesis of complex high-pressure superconducting superhydrides, Phys. Rev. Lett. **128**, 186001 (2022).

[59] Y. Gao, Y. Ma, Q. An, V. Levitas, Y. Zhang, B. Feng, J. Chaudhuri, and W. A. Goddard, III, Shear driven formation of nano-diamonds at sub-gigapascals and 300 K, Carbon **146**, 364 (2019).

[60] E. Clementi and D.-L. Raimondi, Atomic screening constants from SCF functions, J. Chem. Phys. **38**, 2686 (1963).

[61] E. Clementi, D. Raimondi, and W. P. Reinhardt, Atomic screening constants from SCF functions. II. Atoms with 37 to 86 electrons, J. Chem. Phys. **47**, 1300 (1967).